OGLE-2015-BLG-0845L: A low-mass M dwarf from the microlensing parallax and xallarap effects

Zhecheng Hu (胡哲程)[1]★ Wei Zhu (祝伟)[1]†‡ Andrew Gould,[2,3]‡ Andrzej Udalski[4]§
Takahiro Sumi,[5]¶ Ping Chen (陈平),[6] Sebastiano Calchi Novati[7]‡ Jennifer C. Yee[8]‡
Charles A. Beichman,[7]‡ Geoffery Bryden,[9]‡ Sean Carey[7]‡ Michael Fausnaugh[10]‡
B. Scott Gaudi[3]‡ Calen B. Henderson[7]‡ Yossi Shvartzvald[6]‡ Benjamin Wibking[11]‡
Przemek Mróz[4]§ Jan Skowron[4]§ Radoslaw Poleski[4]§ Michał K. Szymański[4]§
Igor Soszyński[4]§ Paweł Pietrukowicz[4]§ Szymon Kozłowski[4]§ Krzysztof Ulaczyk[12]§
Krzysztof A. Rybicki[4,6]§ Patryk Iwanek[4]§ Marcin Wrona[4]§ Mariusz Gromadzki[4]§
Fumio Abe,[13]¶ Richard Barry,[14]¶ David P. Bennett,[14,15]¶ Aparna Bhattacharya,[14,15]¶ Ian A. Bond,[16]¶
Hirosane Fujii,[13]¶ Akihiko Fukui,[17,18]¶ Ryusei Hamada,[5]¶ Yuki Hirao,[19]¶ Stela Ishitani Silva,[20,14]¶
Yoshitaka Itow,[13]¶ Rintaro Kirikawa,[5]¶ Naoki Koshimoto,[5]¶ Yutaka Matsubara,[13]¶ Shota Miyazaki,[21]¶
Yasushi Muraki,[13]¶ Greg Olmschenk,[14]¶ Clément Ranc,[22]¶ Nicholas J. Rattenbury,[23]¶ Yuki Satoh,[5]¶
Daisuke Suzuki,[5]¶ Mio Tomoyoshi,[5]¶ Paul. J. Tristram,[24]¶ Aikaterini Vandorou,[14,15]¶ Hibiki Yama,[5]¶
Kansuke Yamashita[5]¶

Affiliations are listed at the end of the paper.

Accepted XXX. Received YYY; in original form ZZZ

ABSTRACT

We present the analysis of the microlensing event OGLE-2015-BLG-0845, which was affected by both the microlensing parallax and xallarap effects. The former was detected via the simultaneous observations from the ground and Spitzer, and the latter was caused by the orbital motion of the source star in a relatively close binary. The combination of these two effects led to a direct mass measurement of the lens object, revealing a low-mass ($0.14 \pm 0.05 M_\odot$) M-dwarf at the bulge distance (7.6 ± 1.0 kpc). The source binary consists of a late F-type subgiant and a K-type dwarf of $\sim 1.2 M_\odot$ and $\sim 0.9 M_\odot$, respectively, and the orbital period is 70 ± 10 days. OGLE-2015-BLG-0845 is the first single-lens event in which the lens mass is measured via the binarity of the source. Given the abundance of binary systems as potential microlensing sources, the xallarap effect may not be a rare phenomenon. Our work thus highlights the application of the xallarap effect in the mass determination of microlenses, and the same method can be used to identify isolated dark lenses.

Key words: gravitational lensing: micro – methods: data analysis – binaries: general

1 INTRODUCTION

The microlensing effect (Einstein 1936; Paczynski 1986) is able to measure the mass of faint or even dark objects (or stellar systems) independent from their flux (e.g., Gould 1992). So far, the microlensing technique has been used to determine the masses of dozens of isolated objects, including brown dwarfs (e.g., Gould et al. 2009; Zhu et al. 2016; Shvartzvald et al. 2019), low-mass stars (e.g., Chung et al. 2017; Zhu et al. 2017b; Shin et al. 2018; Zang et al. 2020a,b), and stellar remnants (Sahu et al. 2022; Lam et al. 2022; Mroz et al. 2022), as well as another dozens of planetary systems (e.g. Gaudi et al. 2008; Bennett et al. 2015).

Out of thousands of microlensing events that are discovered per year, only a small fraction of them allow one to determine the lens mass directly. This is because, in order to directly determine the lens mass, one needs to measure at least two out of three parameters, namely the angular Einstein radius, the microlensing parallax, and the lens flux (e.g., Yee 2015). The angular Einstein radius measures the characteristic angular size of the microlensing phenomenon and is given by

$$\theta_E \equiv \sqrt{\kappa M_L \pi_{rel}}. \quad (1)$$

Here $\kappa \equiv 4G/(c^2 \mathrm{AU}) \approx 8.14 \mathrm{mas}/\mathrm{M}_\odot$ is a constant, M_L is the lens

★ E-mail: hzc22@mails.tsinghua.edu.cn
† E-mail:weizhu@tsinghua.edu.cn
‡ The Spitzer Team
§ The OGLE Collaboration
¶ MOA Collaboration

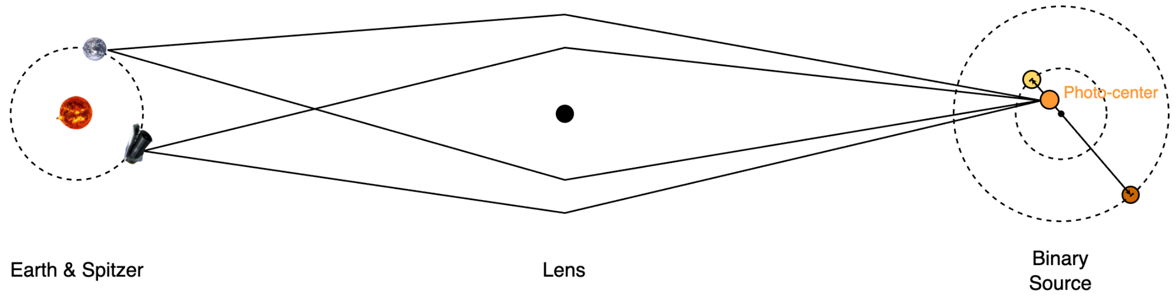

Figure 1. An illustration of the satellite parallax method and the xallarap effect in the microlensing phenomenon. Distances and physical sizes are not to scale. The microlensing source is a binary system, with the yellow circle indicating the primary star (i.e., primary source) and the brown circle indicating the secondary star (i.e., secondary source). The centre of light, namely the photocentre, of the source system is indicated by the orange circle. On the observer plane, Spitzer was in an Earth-trailing orbit and observed the same source simultaneously as the ground-based observatories.

mass, and $\pi_{\rm rel} \equiv {\rm AU}(D_{\rm L}^{-1} - D_{\rm S}^{-1})$ is the lens–source relative parallax (Gould 2000). The microlensing parallax measures the relative parallactic motion scaled to the angular Einstein radius (Gould 1992)

$$\pi_{\rm E} \equiv \frac{\pi_{\rm rel}}{\theta_{\rm E}}. \tag{2}$$

The lens flux measures the observed flux of the lens at the given distance. With a stellar mass–luminosity relation and a given extinction model, the lens flux measurement provides a relation between the lens mass and lens distance, similar to the other two quantities (e.g., Bennett et al. 2015). For faint or dark lenses, the lens flux is usually not detectable, and thus the only option towards a direct mass measurement is through the combination of angular Einstein radius and the microlensing parallax.

Although the microlensing parallax can be measured through the orbital motion of Earth around the Sun (Gould 1992), such an annual parallax effect only applies to microlensing events with relatively long timescales (e.g., Mao et al. 2002; Poindexter et al. 2005; Wyrzykowski et al. 2016). The parameter $\pi_{\rm E}$ of an event could also be measured with at least two well-separated (∼ AU) observatories(Refsdal 1966; Gould 1994b). Between 2014 and 2019, *Spitzer* was used to observe more than five hundred microlensing events, and so far nearly a hundred of them with parallax solutions have been published (e.g., Calchi Novati et al. 2015a; Zhu et al. 2017a).

Several methods are available to measure the Einstein radius, but each has its own limitations. Observing the lens and source separately several years after the event could obtain the lens–source relative motion $\mu_{\rm rel}$, and then $\theta_{\rm E}$ is given by $\theta_{\rm E} = t_{\rm E}\mu_{\rm rel}$, where $t_{\rm E}$ is the Einstein crossing time (e.g. Alcock et al. 2001; Bennett et al. 2015; Gould 2022). The angular Einstein radius can also be determined through the finite source effect, which appears when the source is close to or even crosses the caustic of the lens object/system (Gould 1994a; Witt & Mao 1994; Nemiroff & Wickramasinghe 1994), but in the case of single-lens events, the chance is low to have the finite source effect, except for extremely low-mass lenses such as free-floating planets (e.g., Mróz et al. 2018; Gould et al. 2022). The astrometric microlensing has also been proposed (Hog et al. 1995), and recently realized (Sahu et al. 2022; Lam et al. 2022), as a method to directly measure $\theta_{\rm E}$ during the course of the microlensing event. Additionally, interferometric observations may be able to directly resolve the multiple microlensing images and thus determine $\theta_{\rm E}$ (Delplancke et al. 2001; Dong et al. 2019; Cassan et al. 2022). These latter two methods have not been applied widely because they require high precisions and/or lucky observing conditions.

When the source is in a binary system, its orbital motion around the centre of mass may lead to changes in the relative positions among the microlensing objects, which also revises the light curve (Griest & Hu 1992). This so-called microlensing xallarap effect can also be used to measure the angular Einstein radius (Han & Gould 1997). Specifically, the xallarap parameter, $\xi_{\rm E}$, is related to $\theta_{\rm E}$ via

$$\xi_{\rm E} \equiv \frac{a_{\rm S}}{D_{\rm S}\theta_{\rm E}} = \frac{a_{\rm S}}{\hat{r}_{\rm E}}. \tag{3}$$

Here $a_{\rm S}$ is the semi-major axis of the motion of the source star (or the photocentre of the source binary) around the barycentre of the source binary system, $D_{\rm S}$ is the distance of the source from Earth, and $\hat{r}_{\rm E}$ is the projected Einstein radius in the source plane. Once $\xi_{\rm E}$ and $a_{\rm S}$ are measured, the xallarap effect provides another way to measure $\theta_{\rm E}$.

Given the abundance of stellar binaries (e.g., Duchêne & Kraus 2013), a substantial fraction of events might have been affected by the xallarap effect. Poindexter et al. (2005) searched for the xallarap effect in 22 microlensing events with relatively long ($t_{\rm E} \gtrsim 70$ d) time scales and found that about 23% of them might have been strongly affected by the xallarap effect, although the fraction may be reduced once the shorter but more abundant events are taken into account. The impact of xallarap effect has also been regularly investigated in microlensing events that contain potentially planetary signals (e.g., Furusawa et al. 2013; Miyazaki et al. 2020; Rota et al. 2021; Satoh et al. 2023; Yang et al. 2024; Ryu et al. 2024).

In this work, we present the analysis of the microlensing event OGLE-2015-BLG-0845 . This event shows both xallarap and parallax effects, as illustrated in Figure 1, which allow us to determine directly the lens mass and distance. The observations of OGLE-2015-BLG-0845 are presented in Section 2, the detailed modelings of the event are given in Section 3, and the physical properties of the lens and source are given in Section 4. A brief discussion of the results is given in Section 5.

2 OBSERVATIONS

The microlensing event OGLE-2015-BLG-0845 was first identified by the OGLE-IV collaboration on UT 15:51, 28 April 2015. With equatorial coordinates $({\rm RA, Dec})_{2000}$ = $(18^{\rm h}04^{\rm m}21\overset{\rm s}{.}29, -31^\circ34'50\overset{\prime\prime}{.}0)$ and Galactic coordinates $(l, b)_{2000}$ = $(-0\overset{\circ}{.}25, -4\overset{\circ}{.}82)$, this event was located inside the field BLG514 of OGLE-IV survey and received three observations per day from the 1.3 m Warsaw Telescope at the Las Campanas Observatory in Chile (Udalski 2003; Udalski et al. 2015a). The OGLE observations were mostly taken in the I band, but V band observations were also taken at the cadence of a few days in order to provide colour information of the microlensing source. The OGLE data were reduced using the software developed by Wozniak (2000) and Udalski (2003), which was based on the Difference Image Analysis (DIA) technique of Alard & Lupton (1998).

This event was observed by the Spitzer Space Telescope as part of the 2015 microlensing campaign (Udalski et al. 2015b; Yee et al. 2015; Zhu et al. 2017a). It was selected for Spitzer observations on June 8, 2015, as a "secret event" and then announced as a Spitzer target on June 12, 2015. We refer to Yee et al. (2015) for the details of the observing protocol of the Spitzer microlensing program. The Spitzer observations started on the same date and stopped on July 19, 2015, when the event moved out of the visibility window of Spitzer. There were in total 148 observations taken by Spitzer. All Spitzer observations were reduced by the customized software specifically for the microlensing program Calchi Novati et al. (2015b).

Even OGLE-2015-BLG-0845 was also observed by the Microlensing Observations in Astrophysics (MOA, Bond et al. 2001; Sako et al. 2008). It is called MOA-2015-BLG-277 in the MOA database. Follow-up observations from various small telescopes were also taken for the purpose of detecting planetary signals. Because of the unknown systematics and/or the relatively short time baseline, the MOA data and the follow-up data are not included in the modeling of the parallax and xallarap signals, but they provide useful constraints on the binary lens modeling (see Appendix A).

3 MODELING

The light curve of OGLE-2015-BLG-0845 was first modeled using the standard Paczynski (1986) curve

$$f(t) = f_s A(u[t]) + f_b \tag{4}$$

with the single-lens point-source, or 1L1S [1], microlensing magnification given by

$$A(u) = \frac{u^2+2}{u\sqrt{u^2+4}}. \tag{5}$$

Here f_s and f_b, are the flux of the source star and the flux of the blending object, respectively. The quantity, $u(t)$, is the separation normalized to θ_E between the lens and the source at a given epoch t. For the standard Paczynski (1986) curve,

$$u(t) = \sqrt{\tau^2+\beta^2}, \tag{6}$$

with

$$\tau(t) \equiv \frac{t-t_0}{t_E}, \quad \beta(t) \equiv u_0. \tag{7}$$

Here t_0 is the time when the projected separation between the lens and the source reaches the minimum, u_0 is this minimum separation, and t_E is the Einstein crossing time.

The standard Paczynski (1986) curve cannot fit the light curve of OGLE-2015-BLG-0845 very well, as shown in Figure 2. While these deviations could be modeled by the annual parallax effect reasonably well, it was soon recognized that the parallax parameters from the annual parallax effect did not match those from the satellite parallax effect (Section 3.1). This led to the inclusion of additional effects, including the xallarap effect (Section 3.2). The binary lens, as well as the static binary source model, was also considered, although it could not fit the data as well as the xallarap model (see Appendix A).

In all the modelings, we have made use of the `emcee` package (Foreman-Mackey et al. 2013) to execute a Markov Chain Monte Carlo (MCMC) analysis. The number of walkers and burn-in steps have been adjusted so as to make sure the chain has converged.

3.1 The Tension Between 1L1S Annual and Space-based Parallax Model

The accelerated motion of the Earth can lead to a distortion on the light curve, known as the annual parallax effect (e.g., Gould 1992; Alcock et al. 1995). This distortion adds displacement to the rectilinear motion (Equation 7) of the Paczynski (1986) model

$$(\delta\tau_p, \delta\beta_p) = (\boldsymbol{\pi}_E \cdot \Delta\boldsymbol{s}, \boldsymbol{\pi}_E \times \Delta\boldsymbol{s}). \tag{8}$$

Here $\Delta\boldsymbol{s}$ is the offset of the Earth-to-Sun vector in AU (Gould 2004). The microlensing parallax vector is defined as

$$\boldsymbol{\pi}_E = \frac{\pi_{rel}}{\theta_E}\frac{\boldsymbol{\mu}_{rel}}{\mu_{rel}}, \quad \pi_{rel} = \mathrm{AU}\left(\frac{1}{D_L} - \frac{1}{D_S}\right). \tag{9}$$

Here π_{rel} and $\vec{\mu}_{rel}$ are the relative parallax and the relative proper motion between the lens and source, respectively (Gould 2000).

The microlensing parallax can also be measured through simultaneous observations of the same event from at least two well–separated observatories/satellites (Refsdal 1966; Gould 1994b; Zhu et al. 2017b). The two observatories—namely Spitzer and Earth in the present case—obtain light curves that are different in both the event peak time t_0 and the impact parameter u_0. Making use of the known projected separation between the two observatories on the celestial plane, $D_\perp$, the parallax vector $\boldsymbol{\pi}_E$ can be estimated as

$$\boldsymbol{\pi}_E \approx \frac{\mathrm{AU}}{D_\perp}(\tau_{sat} - \tau_\oplus, \beta_{sat} - \beta_\oplus). \tag{10}$$

Here the subscripts "sat" and "⊕" represent the quantities of the satellite and Earth, respectively.

The two approaches should yield consistent parallax parameters, provided that the deviation from the standard Paczynski (1986) model is indeed due to the annual parallax effect. As shown in Figure 3, for OGLE-2015-BLG-0845 , the constraints on microlensing parallax from fitting OGLE data alone significantly differ from the constraints from the joint fitting of OGLE and Spitzer data, no matter which of the four degenerate solutions is considered. Therefore, other explanations are required to explain the deviation in the light curve from the standard Paczynski (1986) model.

3.2 1L1S Xallarap + Parallax Model

The xallarap effect is the reflection of the orbital motion of the source on the light curve, as is shown in Figure 1. In principle, one should also consider the companion star (hereafter the secondary source) in the light curve modeling. However, the probability is high that the secondary source only contributes a marginal fraction of the total source flux because of the steep relation between stellar mass and luminosity. Therefore, we begin the xallarap modeling by including only one luminous source. For simplicity, the orbit of the source star is assumed to be circular, and the impact of an elliptical orbit is discussed in the section 5.1.

The xallarap effect introduces five new parameters, $(P_\xi, A_\xi, B_\xi, F_\xi, G_\xi)$. Here P_ξ is the orbital period of the

[1] This notation follows the convention that is commonly used in the microlensing literature. The numbers in front of "L" and "S" indicates the numbers of objects in the lens and the source systems, respectively, that directly participate in the microlensing phenomenon in a detectable way. In other words, with "1L" (or "1S") it does not necessarily mean that the source (or lens) object is physically single.

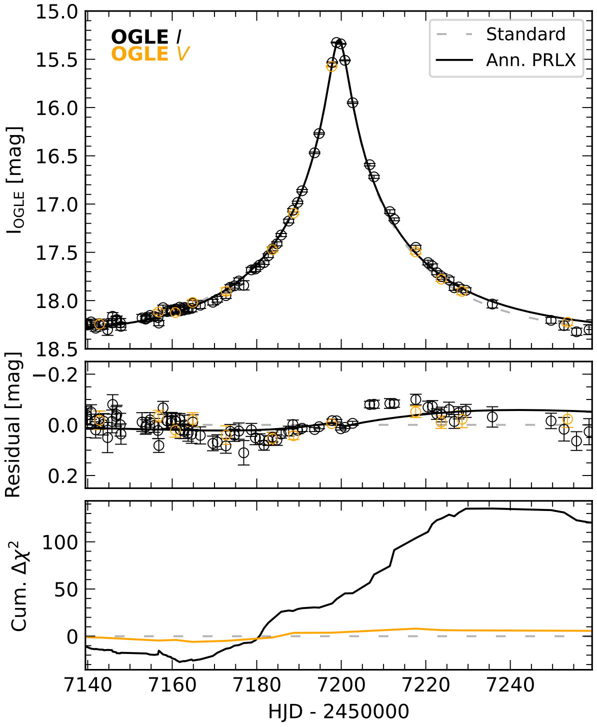

Figure 2. OGLE-IV data of OGLE-2015-BLG-0845 and the best-fit 1L1S standard and annual parallax models. The top panel displays the OGLE I- and V-band data in black and yellow points, respectively. The best-fit standard model and the parallax model are denoted by the grey dashed and the black solid curves, respectively. The middle panel illustrates the residuals of the data and the parallax model with respect to the standard model. The bottom panel shows the cumulative $\Delta\chi^2 \equiv \chi^2_{\rm STD} - \chi^2_{\rm Anu.PRLX}$ between the standard and parallax models as a function of time. Although the best-fit parallax model improved the model χ^2 by > 100 over the standard 1L1S model, there remain long-term variations in the residuals that cannot be well fit.

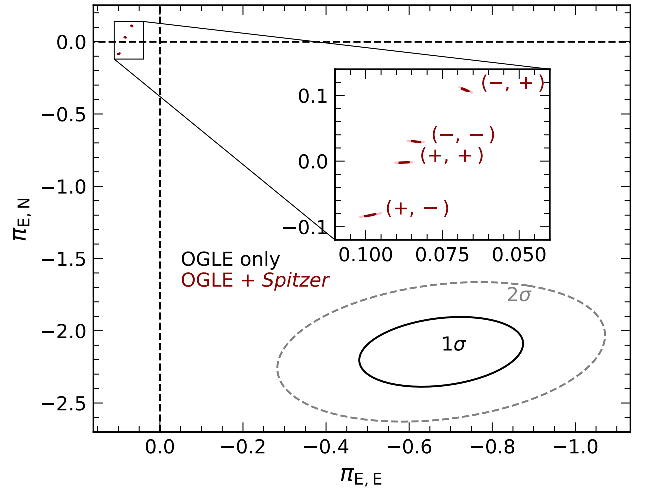

Figure 3. The tension between $\pi_{\rm E}$ as derived by fitting OGLE-only data and joint fitting OGLE and *Spitzer* data of the microlensing event OGLE-2015-BLG-0845 . The 1-sigma regions are shown as dark solid ellipses, while the 2-sigma regions are shown as lighter dashed ellipses. For space-based parallax, all four degenerate solutions are shown while for annual parallax, only the u_0+ solution is shown. The u_0- solution for the OGLE-only fitting is not shown because the $\pi_{\rm E}$ value is close to the positive solutions, which does not change the tension.

source binary, and the other four parameters are variants of the classical Thiele-Innes elements that are widely used in astrometry

$$\begin{cases} A_\xi = \xi_{\rm E}(\cos\phi_\xi \cos(-\theta_\xi) - \sin\phi_\xi \sin(-\theta_\xi)\cos i_\xi) \\ B_\xi = \xi_{\rm E}(\cos\phi_\xi \sin(-\theta_\xi) + \sin\phi_\xi \cos(-\theta_\xi)\cos i_\xi) \\ F_\xi = \xi_{\rm E}(-\sin\phi_\xi \cos(-\theta_\xi) - \cos\phi_\xi \sin(-\theta_\xi)\cos i_\xi) \\ G_\xi = \xi_{\rm E}(-\sin\phi_\xi \sin(-\theta_\xi) + \cos\phi_\xi \cos(-\theta_\xi)\cos i_\xi) \end{cases} \tag{11}$$

Here i_ξ is the orbital inclination, ϕ_ξ is the phase of the source relative to the ascending node at the reference epoch $t_{\rm ref}$, and θ_ξ measures the ascending node relative to the lens–source relative trajectory projected onto the source plane. The amplitude of the xallarap motion, $\xi_{\rm E}$, the semi-major axis of the binary motion scaled to the projected Einstein ring radius, as is defined in Equation 3.

The xallarap effect leads to displacement in the lens-source relative trajectory by the amounts

$$\begin{pmatrix} \delta\tau_{\rm x} \\ \delta\beta_{\rm x} \end{pmatrix} = \begin{pmatrix} A_\xi & F_\xi \\ B_\xi & G_\xi \end{pmatrix} \cdot \Delta\boldsymbol{S} \tag{12}$$

Following the convention in the modeling of the parallax effect (Gould 2004), we have introduced $\Delta\boldsymbol{S}$ to measure the displacement between the actual position of the source under binary motion and an imaginary source under linear motion

$$\Delta\boldsymbol{S} = (t - t_{\rm ref})\boldsymbol{v}_{\rm ref} - [\boldsymbol{S}(t) - \boldsymbol{S}(t_{\rm ref})]. \tag{13}$$

The binary motion of the source, $\boldsymbol{S}(t)$, is given by the circular motion starting from a zero phase with an amplitude of unity, and the velocity vector, $\boldsymbol{v}_{\rm ref}$, is the instantaneous velocity of the source at reference epoch $t_{\rm ref}$.

The distorted lens–source relative trajectory in the presence of both parallax and xallarap effects can be described as

$$\begin{cases} \tau = \tau_{\rm std} + \delta\tau_{\rm p} + \delta\tau_{\rm x} \\ \beta = \beta_{\rm std} + \delta\beta_{\rm p} + \delta\beta_{\rm x} \end{cases}. \tag{14}$$

where $\tau_{\rm std}$ and $\beta_{\rm std}$ describe the trajectory in the standard Paczynski (1986) model.

The best-fit 1L1S xallarap + parallax model is shown in Figure 4, and the best-fit parameters and the associated uncertainties are given in Table 1. The amplitude of the xallarap parameter, $\xi_{\rm E}$, derived from the xallarap model, is also provided in the same table. Note that in this derivation we have ignored the nonuniform prior introduced by the Thiele–Innes parameterization of the xallarap model, and we have confirmed that the values would only be marginally revised if a nonuniform prior were imposed.

The 1L1S Xallarap + Parallax model significantly better describes the light curve by $\Delta\chi^2 \simeq 340$, with respect to the 1L1S Parallax model and removes the tension in parallax constraints between annual and space-based parallax-only models. However, from Table 1, we can see that the $\xi_{\rm E}$ is comparable to the amplitude of u_0. The secondary source, which is fainter and presumably less massive, is expected to experience a binary motion with a larger amplitude and thus produce non-negligible features in the light curve. Therefore, it is reasonable to introduce the secondary source as a luminous component in the microlensing event.

3.3 1L2S Xallarap + Parallax Model

In order to add a luminous secondary source, at least two new parameters are introduced into the modeling: the mass ratio and the wavelength-dependent flux ratio of the secondary source to the primary source, denoted as q_ξ and $q_{{\rm f},\lambda}$, respectively. Note that the flux

Table 1. Parameter values and uncertainties of the best-fit 1L1S and 1L2S xallarap + parallax solutions for OGLE-2015-BLG-0845 .

	1L1S XLRP + PRLX				1L2S XLRP + PRLX			
Solution Type	(+, +)	(+, −)	(−, +)	(−, −)	(+, +)	(+, −)	(−, +)	(−, −)
t_0 [a]	7199.385 ± 0.014	7199.381 ± 0.015	7199.382 ± 0.016	7199.388 ± 0.014	7199.293 ± 0.018	7199.278 ± 0.017	7199.427 ± 0.014	7199.432 ± 0.013
u_0	0.05 ± 0.003	0.0436 ± 0.0025	−0.044 ± 0.003	−0.05 ± 0.003	0.049 ± 0.006	0.046 ± 0.004	−0.043 ± 0.004	−0.047 ± 0.004
t_E (days)	42.1 ± 2.2	47.9 ± 2.4	47.0 ± 2.5	42 ± 2	46 ± 5	49 ± 3	46 ± 4	43 ± 4
$\pi_{\mathrm{E,N}}$	0.0 ± 0.0013	−0.063 ± 0.004	0.084 ± 0.005	0.0231 ± 0.0018	−0.0085 ± 0.0013	−0.074 ± 0.007	0.08 ± 0.007	0.0125 ± 0.0015
$\pi_{\mathrm{E,E}}$	0.077 ± 0.004	0.077 ± 0.004	0.054 ± 0.004	0.074 ± 0.004	0.078 ± 0.008	0.071 ± 0.006	0.065 ± 0.006	0.07 ± 0.006
p_ξ (days)	41 ± 4	46 ± 4	44 ± 5	41 ± 5	74 ± 8	76 ± 7	66 ± 9	63 ± 9
A_ξ (10^{-2})	−0.01 ± 0.003	−0.013 ± 0.004	−0.014 ± 0.005	−0.011 ± 0.003	−0.065 ± 0.017	−0.069 ± 0.016	−0.044 ± 0.012	−0.041 ± 0.012
B_ξ (10^{-2})	−0.011 ± 0.008	−0.018 ± 0.016	0.019 ± 0.018	0.018 ± 0.011	0.16 ± 0.04	0.16 ± 0.03	0.15 ± 0.04	0.14 ± 0.04
F_ξ (10^{-2})	−0.005 ± 0.005	0.003 ± 0.004	−0.001 ± 0.004	−0.007 ± 0.005	0.029 ± 0.019	0.026 ± 0.017	0.02 ± 0.015	0.01 ± 0.016
G_ξ (10^{-2})	−0.061 ± 0.019	−0.062 ± 0.007	0.065 ± 0.008	0.063 ± 0.01	0.07 ± 0.03	0.09 ± 0.03	0.057 ± 0.025	0.06 ± 0.03
q_ξ	—	—	—	—	0.33 ± 0.16	0.28 ± 0.13	0.3 ± 0.2	0.26 ± 0.19
$q_{\mathrm{f,OGLE}}$	—	—	—	—	0.14 ± 0.07	0.11 ± 0.07	0.18 ± 0.08	0.17 ± 0.05
$q_{\mathrm{f,OGLE,V}}$	—	—	—	—	0.15 ± 0.08	0.14 ± 0.08	0.18 ± 0.08	0.17 ± 0.06
$q_{\mathrm{f,Spitzer}}$	—	—	—	—	1.1 ± 0.5	1.2 ± 0.3	0.5 ± 0.3	0.6 ± 0.2
ϕ_ξ^b (deg)	−80 ± 110	−74 ± 25	107 ± 12	107 ± 13	160 ± 6	156 ± 4	162 ± 5	160 ± 5
θ_ξ^b (deg)	97 ± 5	91 ± 4	86 ± 4	81 ± 5	73.8 ± 2.5	74.3 ± 2.0	77.6 ± 1.4	77.2 ± 1.7
i_ξ^b (deg)	82 ± 5	77.7 ± 2.5	101 ± 3	97 ± 4	106 ± 4	106 ± 3	102 ± 4	99 ± 4
ξ_E^b	0.063 ± 0.009	0.064 ± 0.011	0.068 ± 0.014	0.066 ± 0.012	0.18 ± 0.05	0.19 ± 0.04	0.17 ± 0.05	0.16 ± 0.05
Blend fraction	0.19 ± 0.05	0.24 ± 0.04	0.21 ± 0.05	0.13 ± 0.05	0.03 ± 0.14	0.03 ± 0.12	0.11 ± 0.1	0.13 ± 0.09
I_s	18.61 ± 0.06	18.69 ± 0.06	18.64 ± 0.06	18.53 ± 0.06	18.42 ± 0.16	18.38 ± 0.13	18.75 ± 0.15	18.55 ± 0.12
χ^2/dof	1219.38/1126	1193.15/1126	1191.66/1126	1219.89/1126	1148.25/1122	1145.36/1122	1148.09/1122	1143.39/1122

NOTE.
[a] Defined in HJD-2450000. In all fittings, we set the reference time to $t_{0,\mathrm{par}} = t_\mathrm{ref} = 2457200$.
[b] These are derived based on Equations (11).

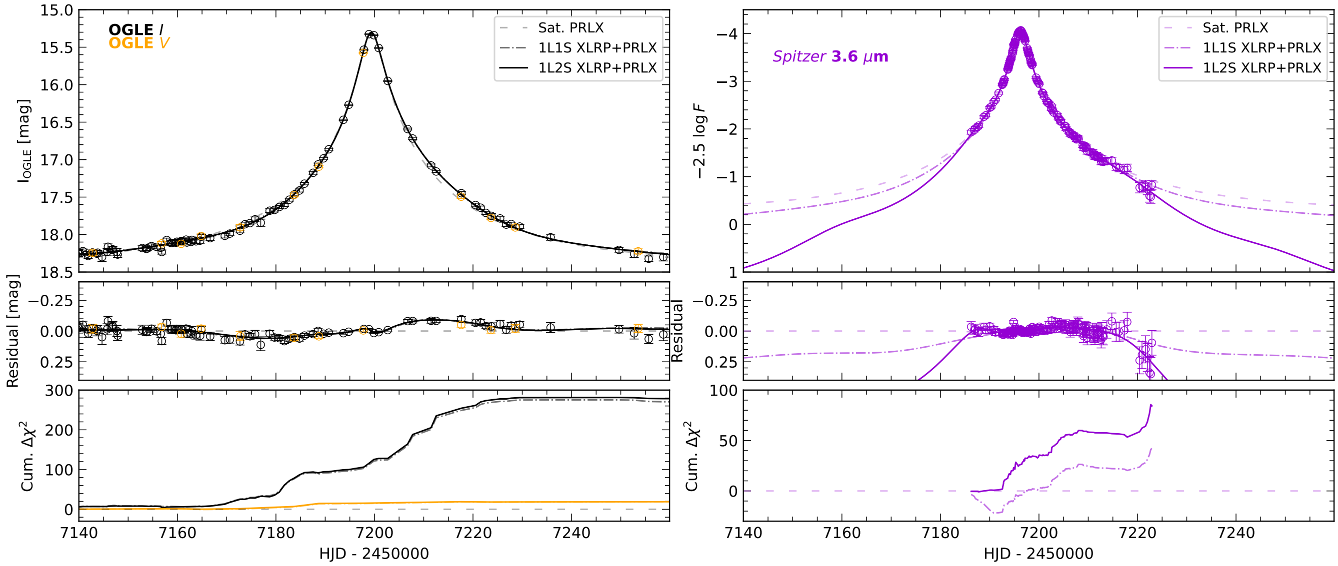

Figure 4. OGLE I and V band light curves (left panels) and *Spitzer* 3.6 μm light curve (right panels) of the microlensing event OGLE-2015-BLG-0845 . In each panel, the best-fit 1L1S parallax model, 1L1S parallax + xallarap model, and the 1L2S parallax + xallarap model are shown as dashed gray line, dash-dotted line, and solid line, respectively. The OGLE V-band data have been aligned to the OGLE I-band data based on the best-fit flux parameters, and the *Spitzer* flux values are shown in logarithmic scale (quasi-magnitudes). The top panels show the observed data and the best-fit models, and the middle panels show the residuals of data and the other models relative to the 1L1S parallax model. In the lower panels, we show the cumulative $\Delta\chi^2$ distribution of the other two models relative to the 1L1S parallax model.

ratio parameter is different for different filters. For this modeling, we have included the I-band and V-band data of the OGLE-IV survey and the Spitzer data, so three flux ratio parameters are included.

The microlensing magnification from this 1L2S model is given by

$$A_{2s,\lambda}(u_1, u_2) = \frac{A(u_1) + q_{f,\lambda} A(u_2)}{1 + q_{f,\lambda}}. \tag{15}$$

Here u_1 (u_2) is the projected separation between the lens and the primary (secondary) source. The position of the primary source is determined in the same way as in Section 3.2. For the secondary source, its positional offset relative to the rectilinear motion is given by

$$\Delta \boldsymbol{S}_2 = (t - t_{\rm ref})\boldsymbol{v}_{{\rm ref},1} + \boldsymbol{S}_1(t_{\rm ref}) - \frac{1}{q_\xi}\boldsymbol{S}_1(t) \tag{16}$$

Here the subscripts 1 and 2 denote the primary and secondary source, respectively. Similar to that for the primary source (Equation 13), the first two terms transform the trajectory from the barycentric frame to the frame centred on the primary source. The last term calculates the orbit of the secondary source, which is $1/q_\xi$ times larger than that of the primary source and on the opposite side of the barycentre. The parallax effect is included in the same way as in the 1L1S case.

As shown in Figure 4 and further detailed in Table 1, the best-fit 1L2S Xallarap+Parallax model provides a better match to the data by $\Delta\chi^2 \simeq 50$, with *Spitzer* data contributing the majority of this improvement. Although this makes the 1L2S model suspicious at first sight, particularly given that some fraction of the *Spitzer* data is known to contain systematics (e.g., Zhu et al. 2017a; Koshimoto & Bennett 2020), there are several pieces of evidence suggesting that the best-fit 1L2S solution is plausible. First, the 1L2S solution is inevitable according to the best-fit 1L1S solution, as has been explained in Section 3.2. Second, the redder secondary source, as inferred from the binary flux ratios in different bandpasses, is consistent with the estimated binary mass ratio directly inferred from the light curve fitting, where more details are described in 4.1, so this binary solution is astrophysically plausible.

Some of the derived parameters in the 1L2S solution appear different from those in the 1L1S solution. In particular, the orbital period of the source binary, P_ξ, changes from ~ 40 d to 60–80 d, and the xallarap parameter, $\xi_{\rm E}$, changes from ~ 0.06 to ~ 0.2. The change in $\xi_{\rm E}$ is due to the different definitions of this parameter in the two models. In the 1L1S model, $\xi_{\rm E}$ is defined by the motion of the centre of light (i.e., photocentre) relative to the centre of mass of the binary, whereas in the 1L2S model the same parameter refers to the motion of the primary source relative to the centre of mass of the binary. The photocentre is closer to the barycentre than the primary source by a factor of $(q_\xi - q_{\rm f})/(q_\xi + q_\xi q_{\rm f})$. Using the values in Table 1, we find this factor to be ~ 0.4. Together with the statistical uncertainties, this can basically explain the change of $\xi_{\rm E}$. The change in the binary orbit period is related to the morphology of the xallarap signal. As shown in the left panel of Figure 4, the xallarap signal appears to be wave-like once the standard 1L1S model is subtracted. This wave-like feature can be approximated by the summation of two lower-frequency (thus longer period) terms, as illustrated in Figure 5. That figure shows the flux variations in the lensing process while the contributions from the two source stars are shown separately. Here the flux variations are given by

$$\Delta F_1 = \frac{f_s}{1 + q_f}(A_1 - 1), \quad \Delta F_2 = \frac{q_f f_s}{1 + q_f}(A_2 - 1) \tag{17}$$

for S1 and S2, respectively.

Table 1 provides the best-fit parameters of the four degenerate solutions, originating from the four-fold parallax degeneracy. These solutions have comparable values of χ^2 and generally consistent values of xallarap parameters. In particular, the source binary is constrained to be nearly edge-on, which is a preferred configuration

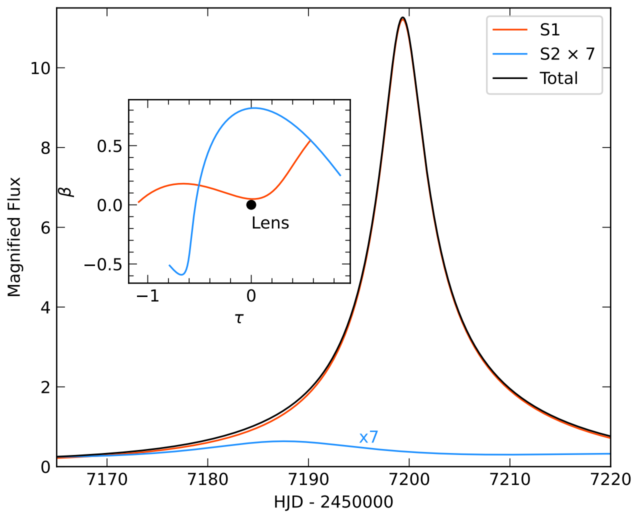

Figure 5. The flux variations of the two source components, S1 and S2, in the 1L2S model. The red and blue curves show the pure flux curve of the S1 and S2, respectively, and the black curve shows the combined result. For illustration purposes, only the $(+,+)$ solution is shown, and the flux variations of S2 have been amplified by a factor of seven. The inset shows the trajectories of the two sources with respect to the lens object. The two sources move from the left to the right.

if one is to verify the 1L2S solution with radial velocity observations (see Section 5.2).

4 PHYSICAL INTERPRETATION

4.1 Source Properties

The angular Einstein radius can be determined by combining the xallarap amplitude, $\xi_{\rm E}$, and the semi-major axis of the primary source, $a_{\rm S}$

$$\theta_{\rm E} = \frac{a_{\rm S}}{D_{\rm S}\xi_{\rm E}}, \tag{18}$$

and $a_{\rm S}$ is related to the mass of the source binary via Kepler's third law

$$\frac{a_{\rm S}}{\rm AU} = \frac{q}{(1+q)^{2/3}}\left(\frac{M_{\rm S}}{M_\odot}\right)^{1/3}\left(\frac{P_\xi}{\rm yr}\right)^{2/3} \tag{19}$$

Here $M_{\rm S}$ is the masses of the primary and q_ξ is the mass ratio. The values of these masses are key in determining $\theta_{\rm E}$, as the xallarap amplitude and the source binary period are both measured in the xallarap modeling.

The mass of the source binary is estimated via the isochrone fitting. To perform this, we first derive the intrinsic colour and magnitude of both sources, following the general method of Yoo et al. (2004). We first obtain the observed colours and magnitudes of both sources through a linear regression based on the 1L2S modeling of OGLE-2015-BLG-0845 . This yields

$$(V-I, I)_{\rm S1} = (1.46 \pm 0.04, 18.65 \pm 0.13) \tag{20}$$

for the primary source and

$$(V-I, I)_{\rm S2} = (1.4 \pm 0.3, 20.6 \pm 0.5) \tag{21}$$

for the secondary source. The above values are derived from the $(+,-)$ solution, i.e., the minimum χ^2 solution, but the difference among the four degenerate solutions in these numbers is statistically negligible.

The centroid of the red clumps is determined to be

$$(V-I, I)_{\rm RC} = (1.972 \pm 0.012, 15.82 \pm 0.07) \tag{22}$$

following the method of Nataf et al. (2013). At the location of OGLE-2015-BLG-0845 , the intrinsic colour and dereddened magnitude of the red clump are

$$(V-I, I)_{\rm RC,0} = (1.06 \pm 0.06, 14.46 \pm 0.04) \tag{23}$$

adapted from Nataf et al. (2013); Bensby et al. (2013), respectively. The reddening and extinction are therefore determined to be

$$(E_{\rm S}(V-I), A_{\rm S}(I)) = (0.91 \pm 0.06, 1.37 \pm 0.08). \tag{24}$$

Together with the observed colours and magnitudes of both sources (Equations 20 and 21) and by assuming the source is at $D_{\rm S} = 8.2 \pm 1.4$ kpc, we determine the intrinsic colour and absolute magnitude of both sources to be

$$(V-I, M_{\rm I})_{\rm S1,0} = (0.54 \pm 0.07, 2.7 \pm 0.3) \tag{25}$$

and

$$(V-I, M_{\rm I})_{\rm S2,0} = (0.5 \pm 0.4, 4.7 \pm 0.5) \tag{26}$$

respectively. For completeness, we have included in Table 2 the measured and derived properties of the source binary for all four degenerate solutions.

The masses of the source stars are estimated based on their positions on the colour–magnitude diagram (CMD) with the `isochrones` package (Morton 2015). This package adopts the MIST (Dotter 2016) isochrone and computes the log-likelihood of five model parameters, namely the equivalent evolutionary phase of both stars, the metallicity, age, and distance of the source system. Given the limited observational constraints, informative priors have been adopted. Specifically, the stellar metallicity is assumed to follow the observed distribution of the bulge microlensing stars from Bensby et al. (2017), and the distance is limited to the range 6.2–10.2 kpc. The posterior distribution is sampled by `emcee` (Foreman-Mackey et al. 2013). The resulting constraints on the stellar masses are shown as the black contours in Figure 6. For illustration purposes, we have shown four typical isochrones with different ages and metallicities that match the positions of the source stars, especially S1, in Figure 7. These isochrones are selected in the following way. First, four representative metallicity values, $(-1.0, -0.5, 0.0, 0.25)$, are selected based on the prior metallicity distribution function (Bensby et al. 2017). Then we determined the age of each isochrone so that it could match the colour and magnitude of S1 well. This process yields an age range from 2.0 Gyr to 7.9 Gyr, and older ages always correspond to lower values of metallicity, which is also consistent with the observed age–metallicity trend of bulge stars (Bensby et al. 2017).

The mass estimates from isochrone fitting also provide us with a way to verify the light curve modeling results. Figure 6 illustrates the masses of binary sources and the mass ratio constraints from light curve modeling (Table 1) for all four degenerate solutions. The isochrone masses generally fall within the 1-σ region of the mass ratio constraint, suggesting that these two sets of estimates are broadly consistent. Given a binary consisting of ~ 1.2 and $\sim 0.9 M_\odot$ stars, the flux ratio in *Spitzer* 3.6μm band is around 0.4. This is in agreement with the flux ratio constraints for the $(-,+)$ and $(-,-)$ solutions and slightly disfavors (by $< 3\sigma$) the $(+,+)$ and $(+,-)$ solutions.

With the mass estimates of source binary stars, the semi-major axis of the source S1 is determined to be 0.4–0.5 au, according to Kepler's third law. Together with the amplitude of the xallarap parameter,

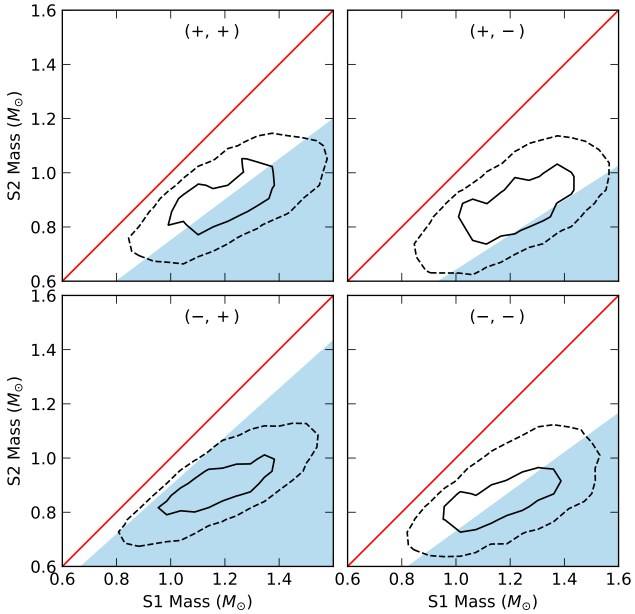

Figure 6. Comparison between the binary mass from the isochrone fitting and the mass ratio q from light curve fitting. The red line represents the $q = 1$ line. The stellar masses determined by isochrone fitting are shown in black contours, with the solid and dashed contours showing the 1 and 2 sigma regions. The light blue shadow regions mark the mass ratio 90% upper limit of each degenerate model.

which is measured from the light curve modeling, we find the angular Einstein radius to be

$$\theta_{\rm E} = 0.125 \left(\frac{a_{\rm S}}{0.2\,{\rm au}}\right)\left(\frac{D_{\rm S}}{8\,{\rm kpc}}\right)^{-1}\left(\frac{\xi_{\rm E}}{0.2}\right)^{-1} {\rm mas}. \tag{27}$$

The exact values and uncertainties of these parameters are included in Table 2 for all four degenerate solutions.

4.2 Mass and Distance of the Lens

Given the constraints on both $\theta_{\rm E}$ and $\pi_{\rm E}$, we now proceed to constrain the mass and distance of the lens object. The mass is given by

$$M_{\rm L} = \frac{\theta_{\rm E}}{\kappa\pi_{\rm E}} \approx 0.15 \left(\frac{\theta_{\rm E}}{0.125\,{\rm mas}}\right)\left(\frac{\pi_{\rm E}}{0.1}\right)^{-1} M_\odot. \tag{28}$$

Similarly, the lens–source relative parallax is given by

$$\pi_{\rm rel} = \pi_{\rm E}\theta_{\rm E} = 0.0125 \left(\frac{\theta_{\rm E}}{0.125\,{\rm mas}}\right)\left(\frac{\pi_{\rm E}}{0.1}\right) {\rm mas}. \tag{29}$$

This value corresponds to a typical bulge lens. Adopting a source distance of $D_{\rm S} = 8.2$ kpc, we find the lens distance to be $D_{\rm L} \approx 7.4$ kpc. Therefore, the lens object of OGLE-2015-BLG-0845 is a low-mass M-dwarf located in the bulge. The exact values and associated uncertainties of the derived mass and distance for all four degenerate solutions are also included in Table 2.

Figure 8 illustrates the constraints on the mass and distance of the lens object for the four degenerate solutions. In addition to the constraints from the angular Einstein radius and the microlensing parallax, we have also shown the upper limit from lens flux. This limit is derived by taking the 90% upper limit on the I-band blending flux and assuming it is due entirely to the lens object. We have adopted the stellar mass–magnitude relations of Pecaut et al. (2012) and Pecaut & Mamajek (2013) and the extinction relation of Bennett et al. (2015),

$$A_{\rm L} = (1 - \exp(-D_{\rm L}/\tau_{\rm dust}))/(1 - \exp(-D_{\rm S}/\tau_{\rm dust}))A_{\rm S}. \tag{30}$$

Here $\tau_{\rm dust} = 0.1{\rm kpc}/\sin({\rm b})$ is the scale length of the dust towards the galactic bulge, with b the Galactic latitude of the source system. For all four solutions, the lens mass and distance, derived from the parallax and angular Einstein radius measurements, are well within the allowed region by the lens flux upper limit.

5 DISCUSSION

5.1 Impact of the Eccentricity

In the 1L2S model with the xallarap effect, we have assumed a circular orbit for the source binary. However, observations have shown that binaries with eccentric orbits are fairly common (e.g., Duchêne & Kraus 2013). In the period range of 10–1000 d, which is relevant for xallarap detection, about half of the binaries have eccentricities above ~0.3 (Raghavan et al. 2010). Therefore, it is necessary to address the impact of eccentric orbits on the derived source and lens properties.

We adopt an eccentric orbit 1L2S model to fit the data. Together with the orbital eccentricity e, the argument of periapsis ω is also introduced to describe the eccentric motion. To avoid over-fit of the weak signal, we fix the orbital eccentricity to values in the range 0.1–0.8 and search the other parameters to minimize the model χ^2. Compared to the circular model, the best χ^2 values of the eccentric orbits are only marginally improved. At $e = 0.3$, the improvement is $\Delta\chi^2 \approx 5$. More eccentric ($e \gtrsim 0.4$) orbits have even worse χ^2 values, and such orbits are disfavored *a priori* at an orbital period of ~ 100 d.

With the introduction of eccentric orbits, model parameters that are relevant to the physical properties of the source and lens objects are not changed substantially. The changes in the flux ratios in different bands and in the mass ratio are all within the uncertainties of the corresponding parameters given in Table 1. With the increasing eccentricity, the xallarap parameter and the orbital period of the source binary may both increase by up to 30–50%, but because these two parameters have opposite effects on the angular Einstein radius, this latter parameter is not changed as much. In the end, the mass and distance of the lens object are only changed by $\lesssim 20\%$, which is small compared to the difference between different degenerate solutions. It does not change the conclusion that the lens is a low-mass M-dwarf in the Bulge.

The inclination remains nearly unchanged with $e \leq 0.3$, but may reach up to 128° at $e = 0.8$. This has some implications for the radial velocity (RV) observations of the source binary, which will be discussed in the next section.

5.2 Source Binary Confirmation

With a baseline magnitude of $I \approx 18.5$ and almost zero blending, the source binary of OGLE-2015-BLG-0845 is potentially accessible by spectroscopic observations from the ground. Such observations can not only confirm but also further refine the derived properties of the source binary (and thus the lens object).

We observed the source with the MagE spectrograph (Marshall et al. 2008) on the 6.5 m Magellan Baade Telescope at Las Campanas Observatory on July 2, 2023. Three exposures, each with 20 min, were taken, and the resulting spectrum has a signal-to-noise ratio (S/N) per resolution of about five. Given the flux ratio of ~ 0.15,

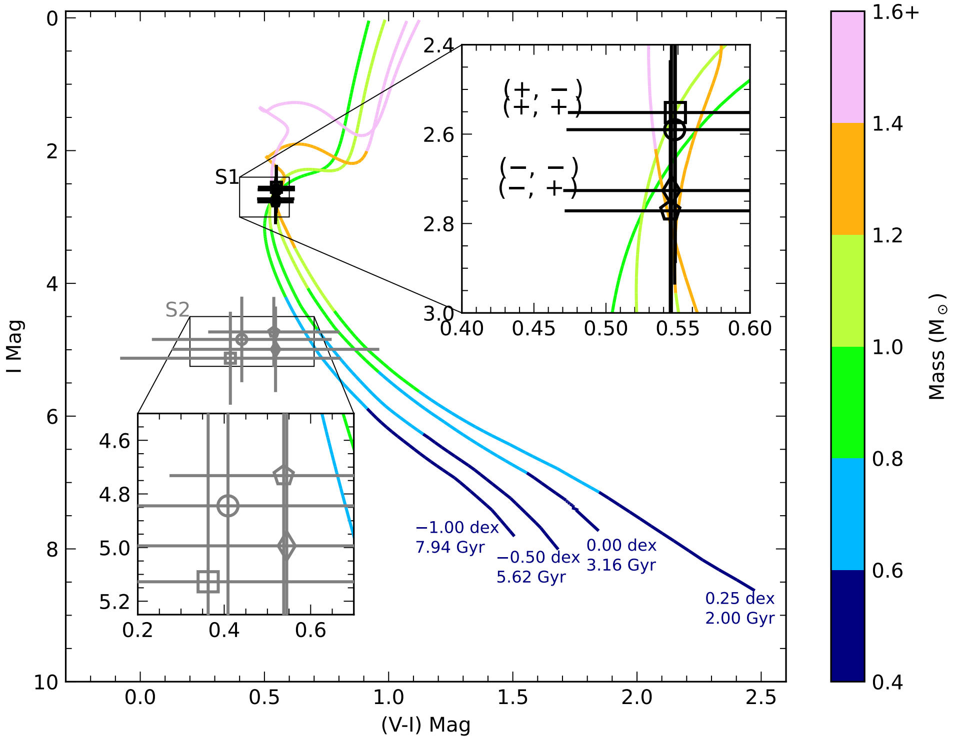

Figure 7. The Colour-Magnitude diagram (CMD) of the four solutions with 1L2S xallarap + parallax model for OGLE-2015-BLG-0845 as well as the isochrones. The four solutions are shown in different markers, i.e., the circle, square, pentagon, and diamond stand for solutions $(+,+)$, $(+,-)$, $(-,+)$, and $(-,-)$, respectively.

Table 2. Physical properties of the source binary and lens object of OGLE-2015-BLG-0845 .

Parameters	$(+,+)$	$(+,-)$	$(-,+)$	$(-,-)$
$(V-I)_{\rm S1,0}$ (mag)	0.55 ± 0.08	0.55 ± 0.07	0.54 ± 0.07	0.55 ± 0.08
$M_{I,\rm S1}$ (mag)	2.6 ± 0.3	2.6 ± 0.3	2.8 ± 0.3	2.7 ± 0.3
$(V-I)_{\rm S2,0}$ (mag)	0.4 ± 0.4	0.4 ± 0.4	0.5 ± 0.3	0.5 ± 0.4
$M_{I,\rm S2}$ (mag)	4.8 ± 0.6	5.1 ± 0.7	4.7 ± 0.5	5.0 ± 0.6
$M_{\rm S1}$ ($M_\odot$)	1.22 ± 0.18	1.23 ± 0.18	1.20 ± 0.18	1.20 ± 0.18
$M_{\rm S2}$ ($M_\odot$)	0.91 ± 0.12	0.88 ± 0.13	0.9 ± 0.11	0.87 ± 0.12
$a_{\rm S}$ (AU)	0.19 ± 0.014	0.189 ± 0.014	0.181 ± 0.015	0.177 ± 0.017
$\theta_{\rm E}$ (mas)	$0.10^{+0.03}_{-0.02}$	$0.091^{+0.022}_{-0.017}$	$0.11^{+0.03}_{-0.02}$	$0.11^{+0.03}_{-0.02}$
$\mu_{\rm rel,geo}$ (mas/yr)	$0.84^{+0.21}_{-0.16}$	$0.78^{+0.18}_{-0.15}$	$0.93^{+0.25}_{-0.19}$	$0.90^{+0.25}_{-0.19}$
$M_{\rm L}$	$0.15^{+0.02}_{-0.02}$	$0.09^{+0.01}_{-0.01}$	$0.13^{+0.02}_{-0.02}$	$0.19^{+0.03}_{-0.03}$
$D_{\rm L}$ (kpc)	$7.68^{+0.06}_{-0.06}$	$7.54^{+0.07}_{-0.07}$	$7.46^{+0.10}_{-0.11}$	$7.72^{+0.06}_{-0.08}$

we expect to see only a single component in the spectra. We compared the observed spectrum with synthetic spectra generated with a stellar atmosphere grid MARCS (Gustafsson et al. 2008) and a radiative transfer code `turbospectrum` (Plez 2012) integrated together by `iSpec` (Blanco-Cuaresma 2019). The observed spectrum can be fitted with the spectra of late F-type subgiants and dwarfs reasonably well, while it disfavors the early F-type as well as the typical G-type stars. This is in agreement with the CMD fitting result.

Future spectroscopic observations are able to measure the RV variations of the source binary (e.g., Ryu et al. 2024). Given the inferred parameters, the RV semi-amplitude is

$$K = 28\ {\rm km/s}\frac{\sin i_\xi}{\sqrt{1-e^2}}\left(\frac{M_{\rm S2}}{0.9M_\odot}\right)\left(\frac{M_{\rm S1}+M_{\rm S2}}{2.1M_\odot}\right)^{-2/3}\left(\frac{P_\xi}{75\ {\rm day}}\right)^{-1/3}. \tag{31}$$

This is large enough for ground-based 10-m telescopes to achieve on a late F-type star. These RV observations will be able to directly measure the orbital eccentricity, which is currently not constrained in the model (Section 5.1). The combination of RV and xallarap can

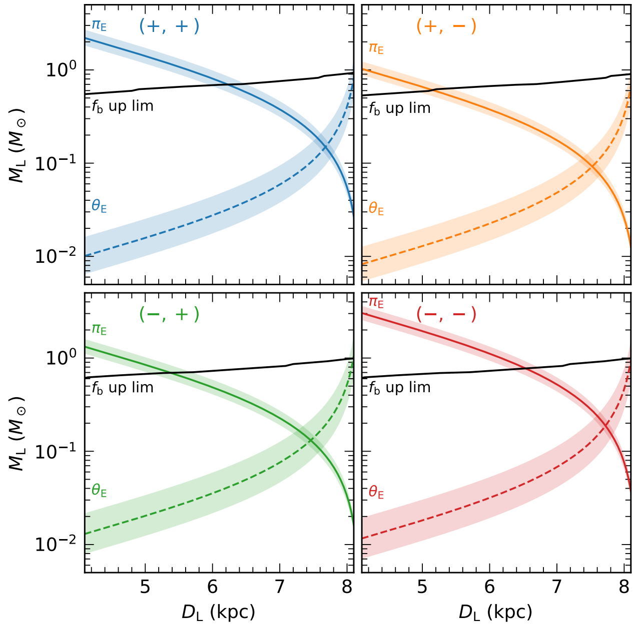

Figure 8. The constraints on the lens mass and distance for OGLE-2015-BLG-0845 , from π_E, θ_E, and lens flux f_b. The four degenerate solutions, $(+,+)$, $(+,-)$, $(-,+)$, and $(-,-)$, are shown in different panels. The black solid line in each panel is the upper limit from the lens flux. The coloured solid line and dashed line with a shaded region around them are the constraints from π_E and θ_E, respectively.

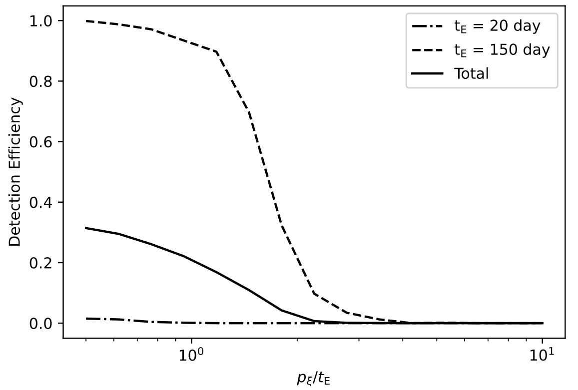

Figure 9. The change of the xallarap effect detection efficiency with regard to p_ξ/t_E ratio when $u_0 = 0.1$. The solid line, dashed line, and dash-dotted line represent the total detection efficiency, as well as the detection efficiency when t_E is 150 or 20 days, respectively.

provide useful constraints on the angular Einstein radius, as has long been pointed out by Han & Gould (1997).

As explained in Section 3.3, the 1L2S model is favored mostly by the *Spitzer* data. It has been argued that the *Spitzer* data might suffer from systematics at some level (e.g., Zhu et al. 2017a; Koshimoto & Bennett 2020), so the verification of the binary source via the RV method also provides an opportunity to further investigate the issues in the *Spitzer* data in this particular event.

5.3 The Detectability of the Xallarap Effect

As demonstrated by the event OGLE-2015-BLG-0845 , the xallarap effect can provide additional information regarding the θ_E parameter and thus has the capability to determine θ_E by utilizing radial velocity measurement or isochrone fitting. Therefore, one wonders how often the xallarap effect appears and is detectable. In particular, under what conditions can the xallarap effect be distinguished from the annual parallax effect?

To answer the above question, we perform the following simplified simulations. We adopt the survey strategy and performance of Karolinski & Zhu (2020) and set the t_0 is at the centre of an observing season. The values of t_E and u_0 were uniformly sampled in the ranges 10–150 days and 0.1–1.0, respectively, which roughly follow the observed distribution of Mróz et al. (2019). The angular Einstein radius is assumed to be 0.55 mas, corresponding to an M-dwarf lens located at 4 kpc. The source binary consists of a primary star of mass $1\,M_\odot$ and a mass ratio of 0.3. This mass ratio corresponds to a luminosity ratio of $\lesssim 1\%$, sufficiently small that we can disregard the light of the secondary source in the light curve modeling. The orbital period of the source binary is sampled from a log-flat distribution between 0.5–10 times t_E, and the orientation of the binary orbit and positions of the source stars are randomized. For each of the simulated light curves, We have performed both parallax and xallarap modelings, and the xallarap signal is considered to be detected if the best-fit $\Delta\chi^2$ between parallax and xallarap models is > 50.

The detection efficiency of the xallarap effect is shown in Figure 9 as a function of the binary orbital period. Source binaries with orbital periods $P \lesssim 2t_E$ are more likely to be detected, as their xallarap signals are difficult to be confused with annual parallax signals. Given the fixed sampling cadence, the detection efficiency therefore drops for shorter timescale events, resulting in an overall frequency of around 1% once the binary period distribution is taken into account. This fraction increases for higher-cadence surveys and events with longer timescales. If we take roughly the same t_E distribution with the events in Poindexter et al. (2005), the detectability of the xallarap effect would be about 18%, consistent with the result of Poindexter et al. (2005) that about 23% of the events with $t_E \gtrsim 70$ d are affected by xallarap effect. Because such long-timescale events are of particular interest in the search for dark lenses (e.g., Lam et al. 2020), the impact of the xallarap effect and its usage in the lens mass determination should be evaluated seriously.

ACKNOWLEDGEMENTS

This work is supported by the National Natural Science Foundation of China (grant No. 12133005 & 12173021) and the CASSACA grant CCJRF2105. We also acknowledge the Tsinghua Astrophysics High-Performance Computing platform for providing computational and data storage resources.

DATA AVAILABILITY

The data underlying this article will be shared on reasonable request to the corresponding author.

REFERENCES

Alard C., Lupton R. H., 1998, The Astrophysical Journal, 503, 325
Alcock C., et al., 1995, The Astrophysical Journal, 454, L125
Alcock C., et al., 2001, Nature, 414, 617
Bennett D. P., et al., 2015, The Astrophysical Journal, 808, 169

Bensby T., et al., 2013, Astronomy & Astrophysics, 549, A147
Bensby T., et al., 2017, Astronomy and Astrophysics, 605, A89
Blanco-Cuaresma S., 2019, MNRAS, 486, 2075
Bond I. A., et al., 2001, Monthly Notices of the Royal Astronomical Society, 327, 868
Calchi Novati S., et al., 2015a, The Astrophysical Journal, 804, 20
Calchi Novati S., et al., 2015b, The Astrophysical Journal, 814, 92
Cassan A., et al., 2022, Nature Astronomy, 6, 121
Chung S. J., et al., 2017, The Astrophysical Journal, 838, 154
Delplancke F., Górski K. M., Richichi A., 2001, Astronomy and Astrophysics, 375, 701
Dong S., et al., 2019, ApJ, 871, 70
Dotter A., 2016, ApJS, 222, 8
Duchêne G., Kraus A., 2013, Annual Review of Astronomy and Astrophysics, 51, 269
Einstein A., 1936, Science, 84, 506
Foreman-Mackey D., Hogg D. W., Lang D., Goodman J., 2013, Publications of the Astronomical Society of the Pacific, 125, 306
Furusawa K., et al., 2013, The Astrophysical Journal, 779, 91
Gaudi B. S., et al., 2008, Science, 319, 927
Gould A., 1992, The Astrophysical Journal, 392, 442
Gould A., 1994a, The Astrophysical Journal, 421, L71
Gould A., 1994b, The Astrophysical Journal, 421, L75
Gould A., 2000, The Astrophysical Journal, 542, 785
Gould A., 2004, The Astrophysical Journal, 606, 319
Gould A., 2022, arXiv e-prints, p. arXiv:2209.12501
Gould A., Loeb A., 1992, The Astrophysical Journal, 396, 104
Gould A., et al., 2009, The Astrophysical Journal, 698, L147
Gould A., et al., 2022, Journal of Korean Astronomical Society, 55, 173
Griest K., Hu W., 1992, The Astrophysical Journal, 397, 362
Gustafsson B., Edvardsson B., Eriksson K., Jørgensen U. G., Nordlund Å., Plez B., 2008, A&A, 486, 951
Han C., Gould A., 1997, The Astrophysical Journal, 480, 196
Hog E., Novikov I. D., Polnarev A. G., 1995, A&A, 294, 287
Karolinski N., Zhu W., 2020, Monthly Notices of the Royal Astronomical Society: Letters, 498, L25
Koshimoto N., Bennett D. P., 2020, AJ, 160, 177
Lam C. Y., Lu J. R., Hosek Matthew W. J., Dawson W. A., Golovich N. R., 2020, ApJ, 889, 31
Lam C. Y., et al., 2022, arXiv:2202.01903 [astro-ph]
Mao S., Paczynski B., 1991, The Astrophysical Journal, 374, L37
Mao S., et al., 2002, MNRAS, 329, 349
Marshall J. L., et al., 2008, in McLean I. S., Casali M. M., eds, Society of Photo-Optical Instrumentation Engineers (SPIE) Conference Series Vol. 7014, Ground-based and Airborne Instrumentation for Astronomy II. p. 701454 (`arXiv:0807.3774`), doi:10.1117/12.789972
Miyazaki S., et al., 2020, The Astronomical Journal, 159, 76
Morton T. D., 2015, isochrones: Stellar model grid package, Astrophysics Source Code Library, record ascl:1503.010 (ascl:1503.010)
Mróz P., et al., 2018, AJ, 155, 121
Mróz P., et al., 2019, The Astrophysical Journal Supplement Series, 244, 29
Mroz P., Udalski A., Gould A., 2022, Systematic Errors as a Source of Mass Discrepancy in Black Hole Microlensing Event OGLE-2011-BLG-0462 (arxiv:2207.10729), doi:10.48550/arXiv.2207.10729
Nataf D. M., et al., 2013, The Astrophysical Journal, 769, 88
Nemiroff R. J., Wickramasinghe W. A. D. T., 1994, ApJ, 424, L21
Paczynski B., 1986, The Astrophysical Journal, 304, 1
Pecaut M. J., Mamajek E. E., 2013, ApJS, 208, 9
Pecaut M. J., Mamajek E. E., Bubar E. J., 2012, ApJ, 746, 154
Plez B., 2012, Turbospectrum: Code for spectral synthesis, Astrophysics Source Code Library, record ascl:1205.004 (ascl:1205.004)
Poindexter S., Afonso C., Bennett D. P., Glicenstein J.-F., Gould A., Szymański M. K., Udalski A., 2005, The Astrophysical Journal, 633, 914
Raghavan D., et al., 2010, The Astrophysical Journal Supplement Series, 190, 1
Refsdal S., 1966, Monthly Notices of the Royal Astronomical Society, 134, 315
Rota P., et al., 2021, The Astronomical Journal, 162, 59
Ryu Y.-H., et al., 2024, The Astronomical Journal, 167, 88
Sahu K. C., et al., 2022, arXiv:2201.13296 [astro-ph]
Sako T., et al., 2008, Experimental Astronomy, 22, 51
Satoh Y. K., et al., 2023, OGLE-2019-BLG-0825: Constraints on the Source System and Effect on Binary-lens Parameters Arising from a Five Day Xallarap Effect in a Candidate Planetary Microlensing Event (arxiv:2307.14274), doi:10.48550/arXiv.2307.14274
Shin I. G., et al., 2018, The Astrophysical Journal, 863, 23
Shvartzvald Y., et al., 2019, The Astronomical Journal, 157, 106
Udalski A., 2003, Acta Astronomica, 53, 291
Udalski A., Szymański M. K., Szymański G., 2015a, arXiv:1504.05966 [astro-ph]
Udalski A., et al., 2015b, The Astrophysical Journal, 799, 237
Witt H. J., Mao S., 1994, The Astrophysical Journal, 430, 505
Wozniak P. R., 2000, Acta Astronomica, 50, 421
Wyrzykowski Ł., et al., 2016, Monthly Notices of the Royal Astronomical Society, 458, 3012
Yang H., et al., 2024, MNRAS, 528, 11
Yee J. C., 2015, The Astrophysical Journal, 814, L11
Yee J. C., et al., 2015, The Astrophysical Journal, 810, 155
Yoo J., et al., 2004, The Astrophysical Journal, 603, 139
Zang W., et al., 2020a, The Astrophysical Journal, 891, 3
Zang W., et al., 2020b, The Astrophysical Journal, 897, 180
Zhu W., et al., 2016, The Astrophysical Journal, 825, 60
Zhu W., et al., 2017a, The Astronomical Journal, 154, 210
Zhu W., et al., 2017b, The Astrophysical Journal, 849, L31

AFFILIATIONS

[1]Department of Astronomy, Tsinghua University, Beijing 10084, China
[2]Max-Planck-Institute for Astronomy, Königstuhl 17, 69117 Heidelberg, Germany
[3]Department of Astronomy, Ohio State University, 140 W. 18th Ave., Columbus, OH 43210, USA
[4]Astronomical Observatory, University of Warsaw, Al. Ujazdowskie 4, 00-478 Warszawa, Poland
[5]Department of Earth and Space Science, Graduate School of Science, Osaka University, Toyonaka, Osaka 560-0043, Japan
[6]Department of Particle Physics and Astrophysics, Weizmann Institute of Science, Rehovot 7610001, Israel.
[7]IPAC, Mail Code 100-22, Caltech, 1200 E. California Blvd., Pasadena, CA 91125, USA
[8]Center for Astrophysics, Harvard & Smithsonian, 60 Garden Street, Cambridge, MA 02138, USA
[9]Jet Propulsion Laboratory, California Institute of Technology, 4800 Oak Grove Drive, Pasadena, CA 91109, USA
[10]Department of Physics and Astronomy, Texas Tech University, 1200 Memorial Circle, Lubbock, TX 79409, USA
[11]Department of Physics and Astronomy, Michigan State University, 567 Wilson Road, East Lansing, MI 48824, USA
[12]Department of Physics, University of Warwick, Gibbet Hill Road, Coventry, CV4 7AL, UK
[13]Institute for Space-Earth Environmental Research, Nagoya University, Nagoya 464-8601, Japan
[14]Code 667, NASA Goddard Space Flight Center, Greenbelt, MD 20771, USA
[15]Department of Astronomy, University of Maryland, College Park, MD 20742, USA
[16]Institute of Natural and Mathematical Sciences, Massey University, Auckland 0745, New Zealand
[17]Department of Earth and Planetary Science, Graduate School of Science, The University of Tokyo, 7-3-1 Hongo, Bunkyo-ku, Tokyo

113-0033, Japan
[18]Instituto de Astrofísica de Canarias, Vía Láctea s/n, E-38205 La Laguna, Tenerife, Spain
[19]Institute of Astronomy, Graduate School of Science, The University of Tokyo, 2-21-1 Osawa, Mitaka, Tokyo 181-0015, Japan
[20]Department of Physics, The Catholic University of America, Washington, DC 20064, USA
[21]Institute of Space and Astronautical Science, Japan Aerospace Exploration Agency, 3-1-1 Yoshinodai, Chuo, Sagamihara, Kanagawa 252-5210, Japan
[22]Sorbonne Université, CNRS, UMR 7095, Institut d'Astrophysique de Paris, 98 bis bd Arago, 75014 Paris, France
[23]Department of Physics, University of Auckland, Private Bag 92019, Auckland, New Zealand
[24]University of Canterbury Mt. John Observatory, P.O. Box 56, Lake Tekapo 8770, New Zealand

APPENDIX A: BINARY LENS INTERPRETATION

An additional companion to the lens object may also lead to distortions in the microlensing light curve (Mao & Paczynski 1991; Gould & Loeb 1992). As long as the source star stays relatively away from the caustics of the binary lens, such distortions are not prominent features and may resemble those produced by the xallarap effect (e.g., Rota et al. 2021; Yang et al. 2024). We therefore carry out 2L1S modeling to make sure the detected signal is indeed caused by the xallarap effect.

In this 2L1S modeling, we exclude the *Spitzer* data but include the MOA data. The latter has a higher cadence, which can be useful in constraining the short-timescale signals arising from the binary lens. To describe the 2L1S model, four new parameters are introduced, namely ρ, α, s, and q. Here, ρ represents the angular size of the source normalized to the angular Einstein radius, α is the angle between the source trajectory and the binary axis, and s and q are the projected separation and mass ratio between the two lens components, respectively. Following a thorough grid search and refined MCMC sampling of the posterior distribution, we only identify one binary lens solution that matches the observed data the best. This best-fit 2L1S model is shown in Figure A1, and the parameter values are given in Table A1 for the purpose of completeness. As shown in Figure A1, the best-fit 2L1S model is not able to explain fully the deviations in the ground-based data, and it is worse than the 1L2S xallarap model by $\Delta\chi^2$ of $\sim$ 130. We therefore exclude the binary lens model as a plausible solution for OGLE-2015-BLG-0845 .

Table A1. Parameters of 1L2S xallarap + parallax solutions for OGLE-2015-BLG-0845

Parameters	(+, +)
t_0 (HJD′)	7199.3746 ± 0.0065
u_0	0.06632 ± 0.00079
t_E (days)	31.80 ± 0.32
ρ	7207.56 ± 0.52
α	0.224 ± 0.015
s	0.136 ± 0.013
q	0.139 ± 0.013
Blend	−0.259 ± 0.023
χ^2/dof	2761.35/2836

NOTE. HJD′=HJD-2450000.

This paper has been typeset from a TEX/LATEX file prepared by the author.

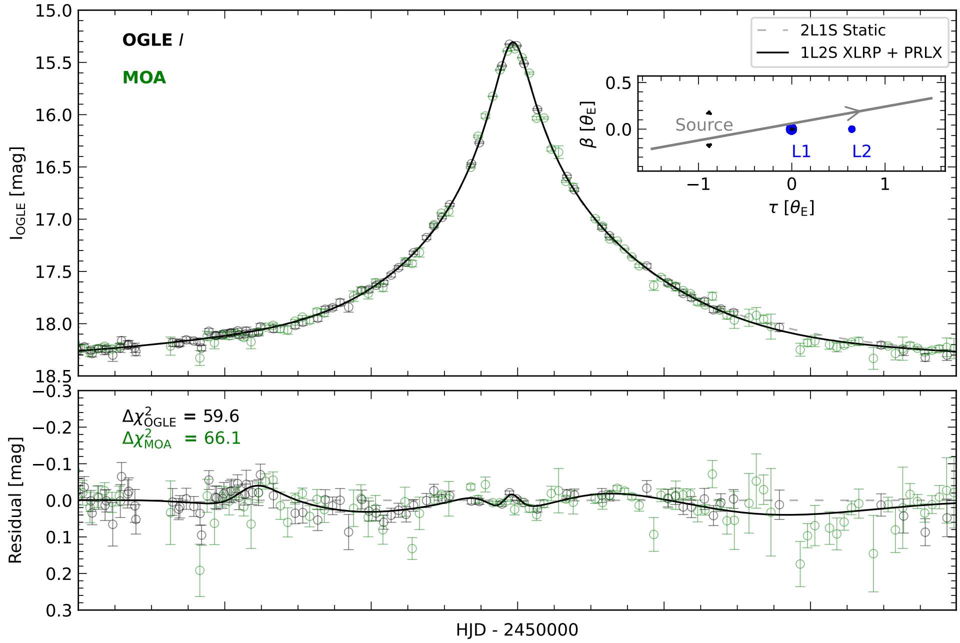

Figure A1. The comparison between the 2L1S model and the 1L2S xallarap + parallax model. The figure description is similar to that of Figure 4. In the figure, the MOA data is binned with a one-day bin size, while the fitting process does not involve any binning. The inset in the upper panel shows the trajectory of the source as well as the caustic curve of the binary lens and the position of the lens.